

Supplemental Material for:
Analog of a quantum heat engine using a single-spin qubit

K. Ono^{1,2}, S. N. Shevchenko^{3,4,5}, T. Mori⁶, S. Moriyama⁷, Franco Nori^{5,8}

¹*Advanced device laboratory, RIKEN,
Wako-shi, Saitama 351-0198, Japan*

²*CEMS, RIKEN, Wako-shi, Saitama 351-0198, Japan*

³*B. Verkin Institute for Low Temperature Physics and Engineering, Kharkov 61103, Ukraine*

⁴*V. N. Karazin Kharkov National University, Kharkov 61022, Ukraine*

⁵*Theoretical Quantum Physics Laboratory,
Cluster for Pioneering Research, RIKEN,
Wako-shi, Saitama 351-0198, Japan*

⁶*Device Technology Research Institute (D-Tech),
National Institute of Advanced Industrial Science and
Technology (AIST), Tsukuba, Ibaraki 305-8568, Japan*

⁷*Department of Electrical and Electronic Engineering,
Tokyo Denki University, Adachi-ku, Tokyo 120-8551, Japan and*

⁸*Department of Physics, The University of Michigan, Ann Arbor, MI 48109-1040, USA*

(Dated: July 20, 2020)

Abstract

In this Supplemental Material (SM) we present details of the device, experiment, and theory.

I. IMPURITY-BASED SPIN QUBIT

TFET-based device.— A tunnel field effect transistor (TFET) includes an n -type source electrode and a p -type drain electrode. Zener tunneling carries on-current, which flows between a channel driven to the p -type (or n -type) electrode by a gate voltage and the n electrode (p electrode), see Fig. S1. This TFET-based device is attracting attention as an ultra-low power consumption device because it enables steeper switching than conventional metal-oxide-semiconductor field effect transistors (MOSFETs). When a deep impurity is introduced into the channel of a TFET having a short channel length, which can be regarded as a gated PIN structure (with an undoped intrinsic semiconductor region between a p -type semiconductor and an n -type semiconductor region), a tunnel current flows through the impurity level even at the off-state of the TFET.

Our TFET-based devices are fabricated in much the same process as conventional MOSFETs. Using a 100 nm thick Si-on-insulator (SOI) wafer with 145 nm thick buried oxide (BOX), the source and drain are formed by shallow donor and acceptor ion implantation, respectively, and are activated by high temperature rapid thermal annealing. Next, Al and N are ion-implanted over the entire region consisting of source, channel, and drain, and annealing is performed for a long time at a relatively low temperature to form Al-N impurity pairs. A MOS gate is formed using TaN high-k / metal and poly-Si.

The electrical conductivity of these devices was probed at a temperature of 1.6 K. The source-drain current I_{SD} was measured while applying the gate voltage V_G and the source-drain voltage V_{SD} . A magnetic field B was applied in parallel to the source-drain current, and by applying a microwave current near the device, an ac magnetic field was generated and used for electron spin resonance (ESR). For the synchronized modulation of both the gate voltage and the microwave frequency, we used a two-channel square-waveform generator. The two square-wave signals have the same frequency and tunable amplitudes and phase difference. One of the square-wave signals is fed to the gate electrode of the device via a DC block capacitor so that the gate voltage is modulated by the square wave with an averaged DC voltage of V_G . The other square-wave signal is fed to an auxiliary input as an analog signal for the frequency modulation (FM) of the MW signal.

Without modulation.— The source-drain voltage V_{SD} and the gate voltage V_G of the device are set to satisfy the spin-blockade condition, where the source-drain current shows

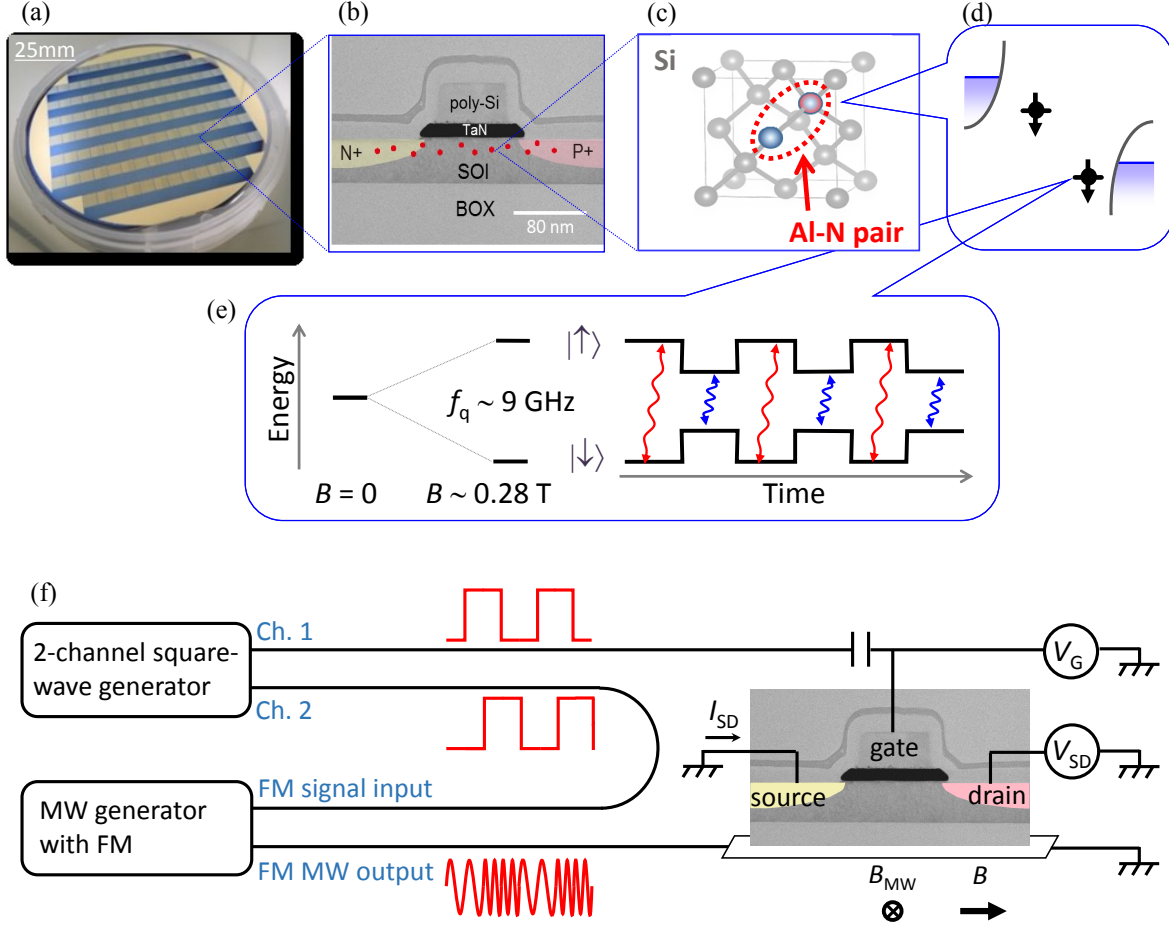


FIG. S1: Overview of device and its operation. The device is fabricated by standard CMOS processing technology with ion-implantations of Al and N, introducing Al-N impurity pairs as deep impurities. (a) Photo of a 4-inch wafer after the ion-implantation processing. (b) Cross-section image by a transmission electron microscope of the TFET-based device. (c) Schematic of an Al-N impurity pair in the unit cell of Si. (d) Schematic diagram of the potential energy landscape for PIN structure in the channel of the TFET with two impurity levels. Electron tunneling via a deep impurity and a shallow impurity exhibits both double-dot-like transport and spin blockade. (e) Schematic of the time evolution of one of the spin qubits. The qubit energy (Zeeman splitting) is modulated with a square-wave form $f_q \pm \delta f_q$. The applied microwave frequency is also modulated with a square-wave form $f_{MW} \pm \delta f_{MW}$. (f) Schematic of the measurement set up. A two-channel square-waveform generator and a MW generator with an FM signal are connected for the double modulation. Schematic wave forms are illustrated as red lines; a square wave from channel 1 (Ch. 1), a square wave from Ch. 2 that has a defined phase difference against the channel 1 signal, and the FM MW signal where its frequency is modulated by the channel 2 signal.

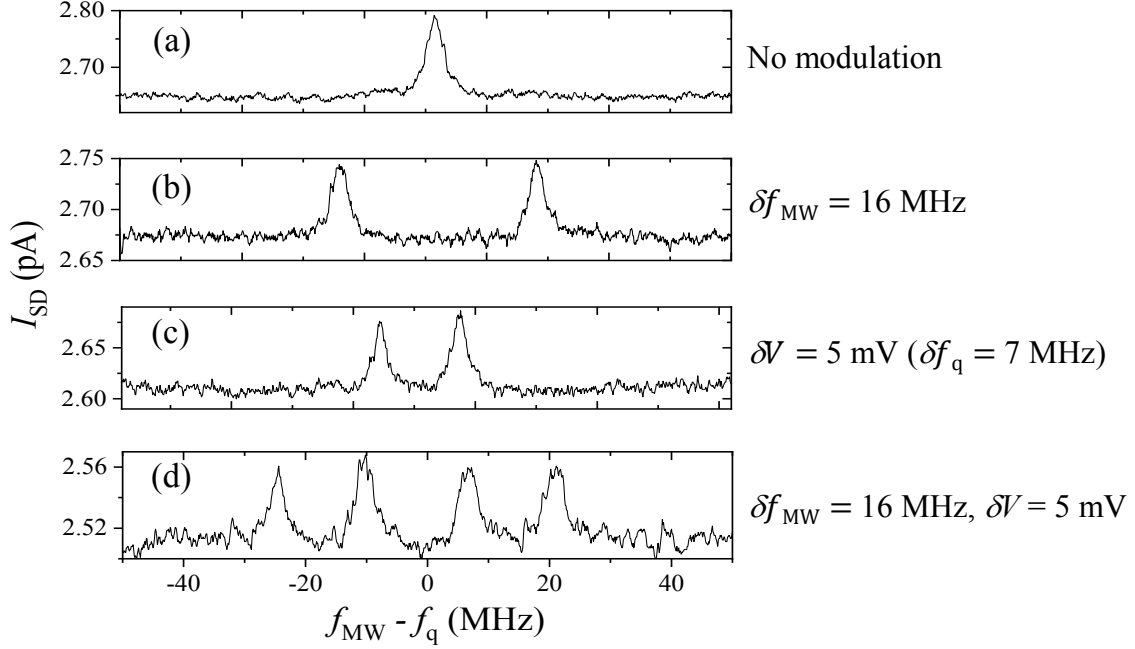


FIG. S2: Electron spin resonance (ESR) signal with and without modulation. (a) without any modulation, one ESR peak (at $f_{\text{MW}} = f_{\text{q}} = 9$ GHz) is observed in the source-drain current I_{SD} of the device in the spin-blockade regime. Two ESR peaks for the modulation of the microwave frequency (b) or for the modulation of the qubit energy (c). Panel (d) presents four ESR peaks when the two modulations are applied simultaneously.

an ESR response. Figure S2(a) shows the ESR signal without any modulation, with a single ESR peak observed where the microwave (MW) frequency f_{MW} matches the qubit frequency $f_{\text{q}} \sim 9$ GHz. The linewidth, or inverse coherence time $(T_2^*)^{-1} = 4$ MHz, is limited by the lifetime of the spin-blockade state, see Ref. [35] of the main text.

Slow amplitude modulation.— We first simultaneously apply the qubit energy modulation, with amplitude $2\delta f_{\text{q}}$, and a microwave frequency modulation (FM), with amplitude $2\delta f_{\text{MW}}$. Both of these modulations have a square-wave form.

In order to realize the condition where the high/low frequency microwave excites the large/small energy gap of the qubit, we tuned the parameters in the following manner. The waveform used for the FM is a square wave with frequency 0.05 MHz, which was set to be much smaller than the inverse coherence time $(T_2^*)^{-1}$. The amplitude of the square wave was set so that the microwave frequency is $f_{\text{MW}} \pm \delta f_{\text{MW}}$. Thus, if we sweep f_{MW} , the two ESR peaks appear at $f_{\text{MW}} - f_{\text{q}} = \pm \delta f_{\text{MW}}$ [Fig. S2(b)].

Then we also turn-on the qubit energy modulation by adding a square-wave modulation on V_G . By increasing the modulation amplitude δV_G from zero, each of the two ESR peaks is further split into two, and thus in total four peaks appear. Those four peaks correspond to four combinations where the qubit with energy $f_q \pm \delta f_q$ is excited by microwaves with frequency $f_{MW} \pm \delta f_{MW}$ [Fig. S2(d)]. Figure 2(b) of the main text shows the evolution of the ESR peaks increasing δV_G . The crossing of the lines of the ESR peaks appear at $\delta V_G = 11$ mV, where we see three peaks instead of four. The three peaks correspond to these three situations:

(1) the qubit with frequency $(f_q - \delta f_q)$ is excited by microwaves with frequency $(f_{MW} + \delta f_{MW})$;

(2) the qubit with $(f_q - \delta f_q)$ is excited by the microwave with $(f_{MW} - \delta f_{MW})$ and, at the same time, the qubit with $(f_q + \delta f_q)$ is excited by the microwave with $(f_{MW} + \delta f_{MW})$; and

(3) the qubit with $(f_q + \delta f_q)$ is excited by the microwave with $(f_{MW} - \delta f_{MW})$. Thus, at the center peak (peak at the crossing) δf_{MW} is matched to δf_q . Now δV_G can be converted to δf_{MW} , as shown in the left axis of Fig. 2(b) of the main text.

II. THEORY OF AMPLITUDE- AND FREQUENCY-MODULATED SINGLE SPIN

A. Hamiltonian and master equation

We describe our device as a modulated and driven quantum two-level system with the pseudo-spin Hamiltonian

$$H(t) = B_z(t)\sigma_z/2 + B_x(t)\sigma_x/2. \quad (\text{S1})$$

To be more precise, we consider a single 1/2-spin with a fast microwave driving and a slow rf modulation of both amplitude and frequency. The longitudinal part is defined by the Zeeman splitting, $B_z(t) = g(t)\mu_B B$. The time-dependent gate voltage changes the g -factor by a small value and we have

$$B_z/\hbar = \omega_q + \delta\omega_q \cdot s(t), \quad \delta\omega_q \ll \omega_q, \quad (\text{S2})$$

Parameter	Description	Value or Range
ω_q	$= 2\pi f_q$, ESR frequency; this is defined by the magnetic field, $\omega_q \propto B$	$f_q = 9.0$ GHz at $B = 0.28$ T
$\delta\omega_q$	$= 2\pi\delta f_q$, amplitude of energy-level modulation; defined by the gate voltage modulation, $\delta\omega_q \propto \delta V$	$\delta f_q = 16$ MHz at $\delta V = 12$ mV
Ω	square-modulation frequency	$\Omega \in [0.05, 50]$ MHz $\cdot 2\pi$
ω_{MW}	$= 2\pi f_{\text{MW}}$, driving MW frequency	$\omega_{\text{MW}} = \omega_q - \Delta\omega$, $ \Delta\omega \leq 50$ MHz $\cdot 2\pi$
$\delta\omega_{\text{MW}}$	amplitude of frequency modulation	$\delta\omega_{\text{MW}} = 32$ MHz $\cdot 2\pi$
G	driving amplitude; this is defined by the microwave power at the MW-generator output, $G \propto \sqrt{P_{\text{MW}}}$	$G = 1$ MHz $\cdot 2\pi$ at $P_{\text{MW}} = 7$ dBm
ϕ	phase shift	$\phi \in [0, 360]$ degrees

TABLE I: Description of the parameters controlling our driven and modulated single-spin qubit

where $\omega_q = 2\pi f_q$ represents the ESR frequency, $\delta\omega_q$ describes the *amplitude modulation*. In this work, we consider a square-wave modulation with the signal

$$s(t) = \text{sgn}[\cos \Omega t]. \quad (\text{S3})$$

The transverse part of the Hamiltonian is defined by the frequency-modulated MW voltage applied to the substrate,

$$\begin{aligned} B_x/\hbar &= 2G \cos[\omega_{\text{FM}}(t)t], \\ \omega_{\text{FM}}(t) &= \omega_{\text{MW}} + \delta\omega_{\text{MW}} \cdot s_\phi(t), \\ s_\phi(t) &= \text{sgn}[\cos(\Omega t + \phi)], \end{aligned} \quad (\text{S4})$$

with amplitude G and microwave circular frequency $\omega_{\text{MW}} = 2\pi f_{\text{MW}}$. The modulation is assumed to be slow, i.e. $\Omega \ll \omega_{\text{MW}}$, and with a small amplitude, $\delta\omega_{\text{MW}} \ll \omega_{\text{MW}}$, where $\delta\omega_{\text{MW}}$ describes the *frequency modulation*. The theoretical and experimental parameters are collected in Table I.

After the unitary transformation $U = \exp(-i\omega_{\text{MW}}\sigma_z t/2)$ and the rotating-wave approxi-

mation, as in Refs. [35, 43, 45] of the main text, we obtain

$$H_1 = \frac{\hbar}{2} \left[\Delta\omega + \tilde{f}(t) \right] \sigma_z + \frac{\hbar G}{2} \sigma_x, \quad (\text{S5})$$

$$\tilde{f}(t) = \delta\omega_q \cdot s(t) - \delta\omega_{\text{MW}} \cdot s_\phi(t), \quad (\text{S6})$$

where $\Delta\omega = \omega_q - \omega_{\text{MW}} = 2\pi (f_q - f_{\text{MW}})$.

Then, the upper-level occupation probability P_+ is readily obtained from the stationary solution of the Bloch equations:

$$P_+ \left(\Delta\omega, \frac{\delta\omega_q}{\Omega} \right) = \frac{1}{2} \sum_{k=-\infty}^{\infty} \frac{G_k^2(\delta\omega_q/\Omega)}{G_k^2(\delta\omega_q/\Omega) + \frac{T_2}{T_1} (\Delta\omega - k\Omega)^2 + \frac{1}{T_1 T_2}}, \quad (\text{S7})$$

where $G_k(x) = G |\Delta_k(x)|$, which can be interpreted as the dressed qubit gap, modulated by the function $\Delta_k(x)$

$$\Delta_k = \int_0^1 d\tau \exp \left[-i2\pi k\tau + i \int_0^\tau d\tau' \tilde{f}(\tau') \right]. \quad (\text{S8})$$

The relaxation and decoherence times are denoted as T_1 and T_2 , respectively.

It is straightforward to calculate Δ_k using Eq. (S8) with the integrand $\tilde{f}(\tau)$ defined by Eq. (S6). The resulting expression for Δ_k consists of four terms, which have the denominators $-k \pm x \pm w$, respectively, with $x = \delta\omega_q/\Omega$ and $w = \delta\omega_{\text{MW}}/\Omega$. This defines the characteristic k 's for each term. And, respectively, the absolute values of Δ_k for these four terms are the following

$$|\Delta_k| = \left| \frac{\sin \left[\frac{\pi-\phi}{2} (k \mp (x-w)) \right]}{\pi (k \mp (x-w))} \right|, \quad \left| \frac{\sin \left[\frac{\phi}{2} (k \mp (x+w)) \right]}{\pi (k \mp (x+w))} \right|. \quad (\text{S9})$$

Consider now the limiting case $\Omega \rightarrow 0$, which describes the incoherent-regime resonances at $\Omega < 2T_2^{-1}$, as detailed in Ref. [35] of the main text. We then expect resonances along the lines

$$\Delta\omega = k\Omega = \pm\delta\omega_q \pm \delta\omega_{\text{MW}}. \quad (\text{S10})$$

An analysis of the four relations from Eq. (S9) in the limit $\Omega \rightarrow 0$ gives for $\phi \in [0, \pi]$

$$|\Delta_k| \simeq \frac{\phi}{2\pi} \quad \text{for } k \simeq \pm (\delta\omega_q + \delta\omega_{\text{MW}}), \quad (\text{S11})$$

$$|\Delta_k| \simeq \frac{\pi - \phi}{2\pi} \quad \text{for } k \simeq \pm (\delta\omega_q - \delta\omega_{\text{MW}}). \quad (\text{S12})$$

The above equations are useful for describing the experimental results, as detailed in the next Section.

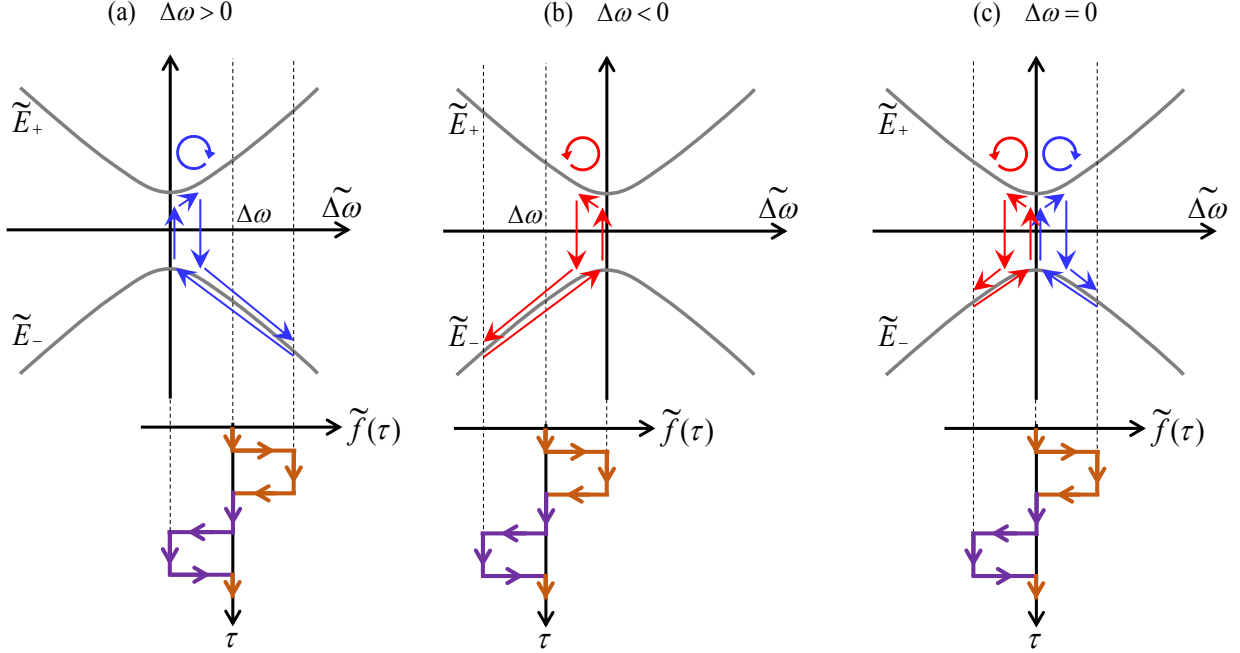


FIG. S3: Schematic of the refrigerator-like and engine-like cycles. The dressed energy levels \tilde{E}_{\pm} are plotted as a function of the modulation-defined frequency offset $\widetilde{\Delta\omega}$. The modulation $\tilde{f}(t)$ allows the system to oscillate between two limiting values, with a possible excitation at the avoided-level crossing and the subsequent relaxation. This is illustrated here for the incoherent regime, $\Omega/2\pi < 2T_2^{-1}$.

B. Dressed states and heat-engine-like cycles

Equation (S5) describes the qubit dressed by the microwave signal. The respective eigenstates are

$$\tilde{E}_{\pm} = \pm \frac{\hbar}{2} \sqrt{G^2 + \widetilde{\Delta\omega}^2}, \quad (\text{S13})$$

where $\widetilde{\Delta\omega} = \Delta\omega + \tilde{f}(t)$. In this way, the time dependence in $\tilde{f}(t)$ results in varying the distance between the dressed-state energy levels $\tilde{E}_+ - \tilde{E}_-$. The energy levels are plotted in Fig. S3. Then, we consider the dynamics forced by the modulation $\tilde{f}(t)$, around $\widetilde{\Delta\omega} = \Delta\omega$.

In figure S3, we consider the symmetric case with $\delta\omega_q = \delta\omega_{\text{MW}}$, which corresponds to the horizontal dashed line in Fig. 2(b) of the main text. Then the modulation $\tilde{f}(t)$ takes three values, 0 and $\pm 2\delta\omega_q$. We colour the curve for $\tilde{f}(t)$ in brown when this corresponds to the large-energy-gap half-period and in purple when this corresponds to the small-energy-gap half-period.

Then we consider three situations in Fig. S3(a-c), for $\Delta\omega = 2\delta\omega_q$, $-2\delta\omega_q$, and 0, respectively. In the situations (a) and (b), the qubit is excited during the small-energy-gap and large-energy-gap stages, respectively. For the incoherent regime, when $\Omega/2\pi < 2T_2^{-1}$, the system relaxes to the ground-state, and its evolution is shown by the blue and red trajectories. In terms of Fig. 1 of the main text, these correspond to the refrigerator-like and engine-like cycles. We mimic this by the blue and red round arrows in Fig. S3(a,b).

In the symmetric situation in Fig. S3(c), there are two cycles, both clockwise and counter-clockwise, during one modulation period. We emphasize that there is no crosstalk between the two cycles, since the relaxation is fast in the incoherent regime. In contrast, when increasing the modulation frequency so that $\Omega/2\pi \gtrsim 2T_2^{-1}$, i.e. going to the coherent regime, such cycles start to overlap. Essentially, *such superposition of the two cycles results in the constructive or destructive interference* with increased or suppressed upper-level occupation probability. We consider these interference fringes in detail both in the main text and below.

III. RESULTS

A. Experiments

Measurements as in Fig. 2(b) in the main text, for various ϕ , are shown in Fig. S4(a-e). In Fig. S4(f-j) we demonstrate the results of calculations related to the experimental ones in Fig. S4(a-e), respectively. Details of the calculations are described in the next subsection.

The dependence of the source-drain current I_{SD} on the square-wave modulation frequency Ω and the microwave frequency f_{MW} for $\delta f_{MW} = 0$ and $\delta V = 0$ are shown in Fig. S5(a) and Fig. S5(b), respectively.

Figure S6 shows measurements as in Fig. 3(b) in the main text but with different parameters, as written in each figure. We note that due to the delay of the two modulation signals, the phase difference depends on the modulation frequency within the MHz regime. Thus we redefine the $\phi = 0$ position so that the intensity plot image becomes symmetric.

These experimental data are all reproduced by our calculations. Figure S7 shows such calculated results, where the modulation-frequency dependence corresponds to Fig. S6(a-e); see details in the next subsection.

We extract the period of the notches from the data in Fig. S6 and summarize them in

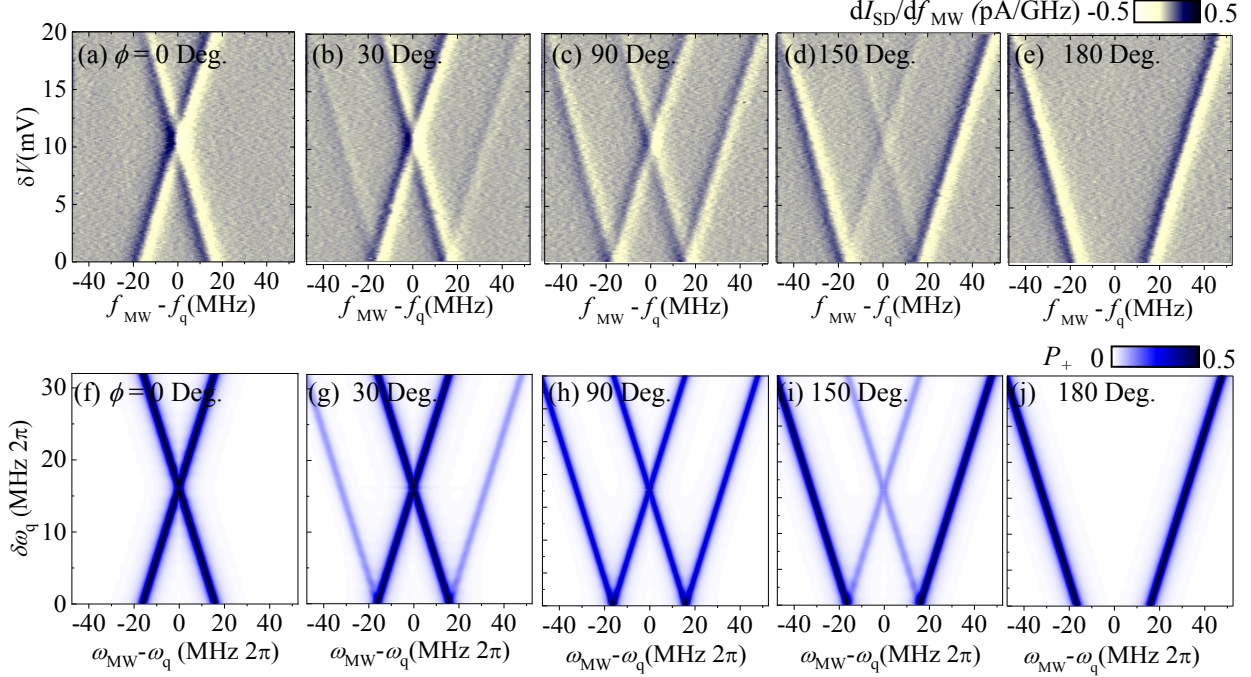


FIG. S4: The experimental source-drain current I_{SD} , top row, and the theoretical upper-level occupation probability P_+ , bottom row, as a function of the energy-level modulation amplitude $\delta\omega_q = \delta\omega_q(\delta V)$ and the microwave frequency $\omega_{MW} = 2\pi f_{MW}$. The data are similar to the ones in Fig. 2(b) of the main text, for various phase shifts ϕ ; the parameters are the same as in Fig. 2 of the main text, except of ϕ . The panels (a-e) and (f-j) show the experiment and calculations, respectively. For $\phi = 0$ the in-phase condition is met at $\delta V = 12$ mV, where $\delta f_q = \delta f_{MW}$, while the out-of-phase condition is met at $\delta V = 12$ mV and $\phi = 180$ deg.

Fig. S8, showing excellent agreement between the experiments and calculations.

Figure S9(b) shows one example of the measurements as in Fig. S4(a) ($\phi = 0$) for the fast modulation frequency $\Omega/2\pi = 2$ MHz. The X-shaped pattern in S9(b), similar to the one in Fig. S4(a), was obtained; but there are weak ripples around the pattern. Note that if ϕ is set at a notch [$\phi = 11$ deg., Fig. S9(c)], the X-shaped pattern shows a weak avoided crossing in the middle of the green dashed horizontal line in Fig. S9(c).

B. Theory

Using formulas (S7) and (S9) we can *quantitatively* describe the experimental results.

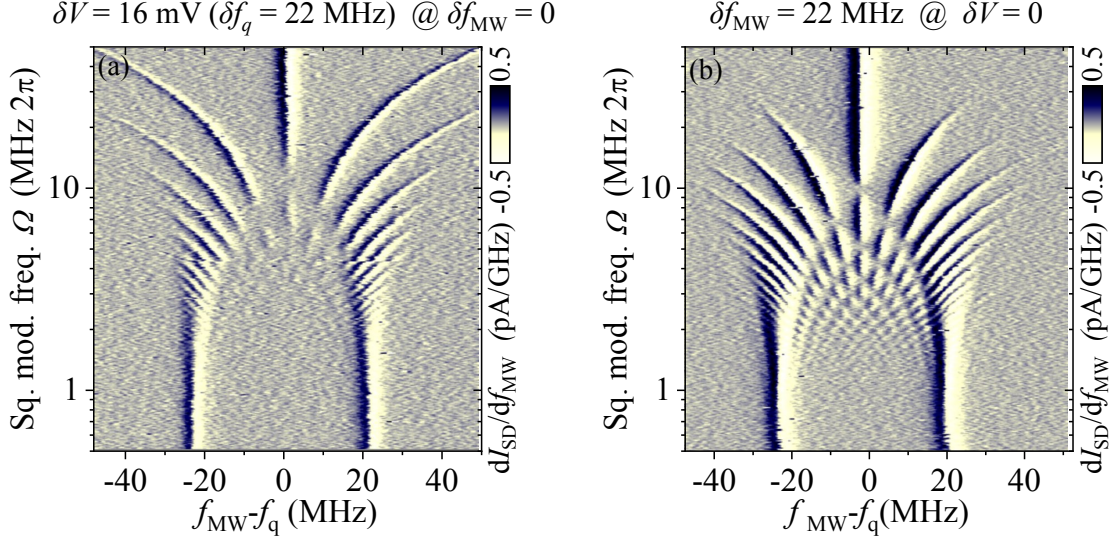


FIG. S5: Dependence of the source-drain current I_{SD} on the square-wave modulation frequency Ω and the microwave frequency f_{MW} for $\delta f_{MW} = 0$ (a) and $\delta V = 0$ (b). The amplitude of the modulation δV_G is fixed to 8 mV, which corresponds to $\delta f_q = 22$ MHz. The interference pattern is the same as discussed in Ref. [35] of the main text and agrees with the calculations. This ensures that square-wave signals up to 50 MHz can be applied to the gate without significant deformation of the waveform. In (b) the FM frequency of the microwave changes from 0.5 to 50 MHz. The amplitude δf_{MW} of the FM is fixed to 22 MHz. The interference pattern shows a cut-off of the sideband peaks for modulation frequencies larger than 10 MHz. Thus, we limit the FM modulation up to 5 MHz in the following measurements.

1. Incoherent regime

Consider, first, the incoherent regime, with $\Omega < 2T_2^{-1}$. This is described by the four possible resonance lines in Fig. 2 of the main text and Fig. S4, where the lower row was plotted making use of Eqs. (S7) and (S9). We note that the height and the width of the lines are defined by the phase shift ϕ .

In order to better understand the origin of the four lines in the W-shaped pattern in Fig. S4, consider now Eqs. (S11, S12). Then, at $\phi = 0$, the width of the lines, described by Eq. (S11), tends to zero, and we have two lines only at

$$\Delta\omega = \pm(\delta\omega_q - \delta\omega_{MW}), \quad (\text{S14})$$

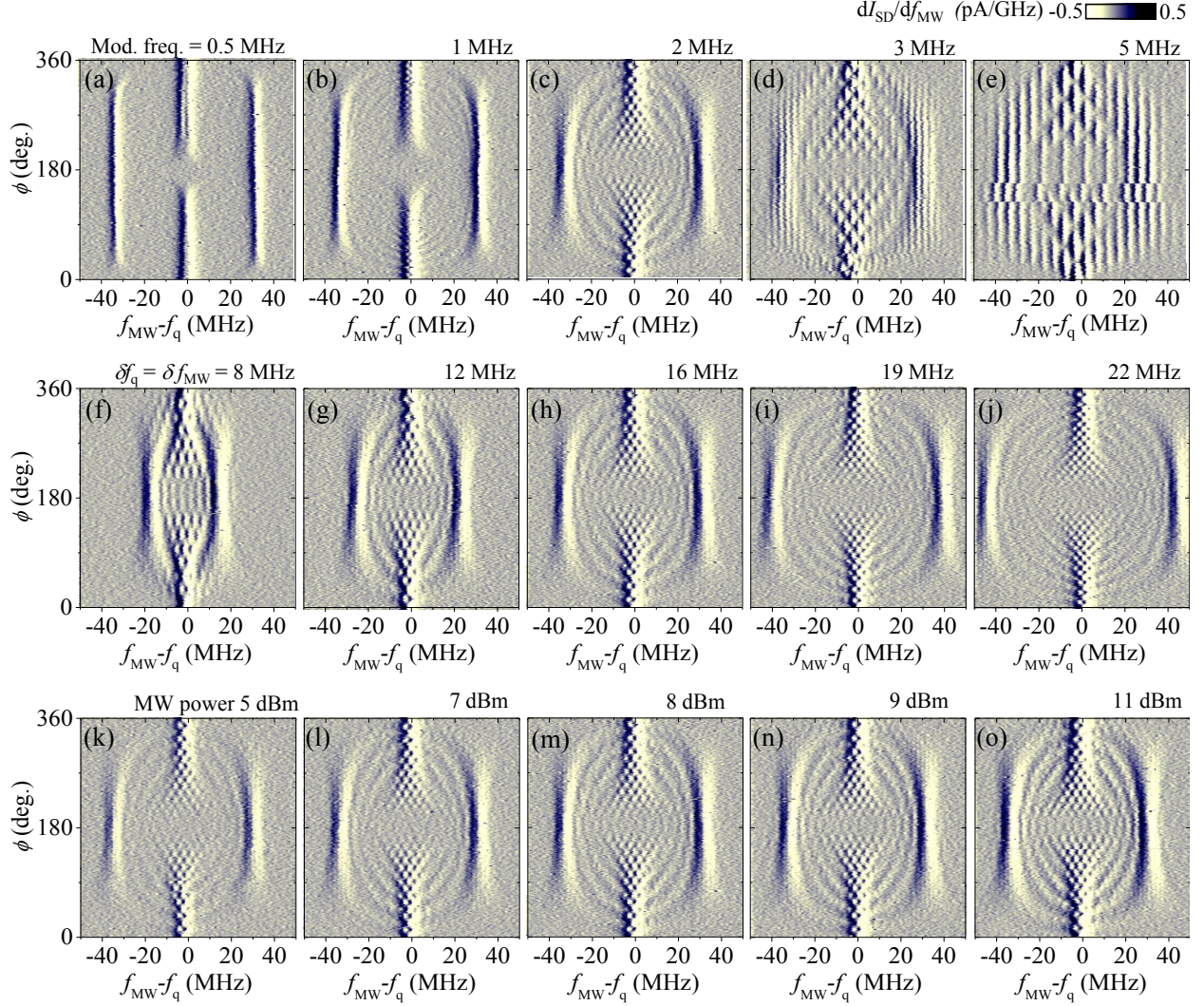


FIG. S6: Summary of the phase ϕ dependence, as in Fig. 3 of the main text, for various modulation frequencies Ω (a-e), various modulation amplitudes δf_{MW} (f-j), and various microwave powers P_{MW} (k-o). Parameters are the same as in Fig. 3, except the ones shown in this figure. For (f-j) similar measurements as in Fig. 2 were performed when $\delta f_{\text{q}} = \delta f_{\text{MW}}$.

which corresponds to the X-shaped lines in Fig. S4(f). They intersect at $\delta\omega_{\text{q}} = \delta\omega_{\text{MW}}$, which, importantly, can be useful for calibration of the power. Next, at $\phi = \pi$, the width of the lines, described by Eq. (S12), tends to zero, and we have two other lines, along

$$\Delta\omega = \pm(\delta\omega_{\text{q}} + \delta\omega_{\text{MW}}), \quad (\text{S15})$$

which corresponds to the V-shaped lines in Fig. S4(j). For other values of ϕ , we have all the four lines. Their widths become equal for $\phi = \pi/2$, Fig. S4(h).

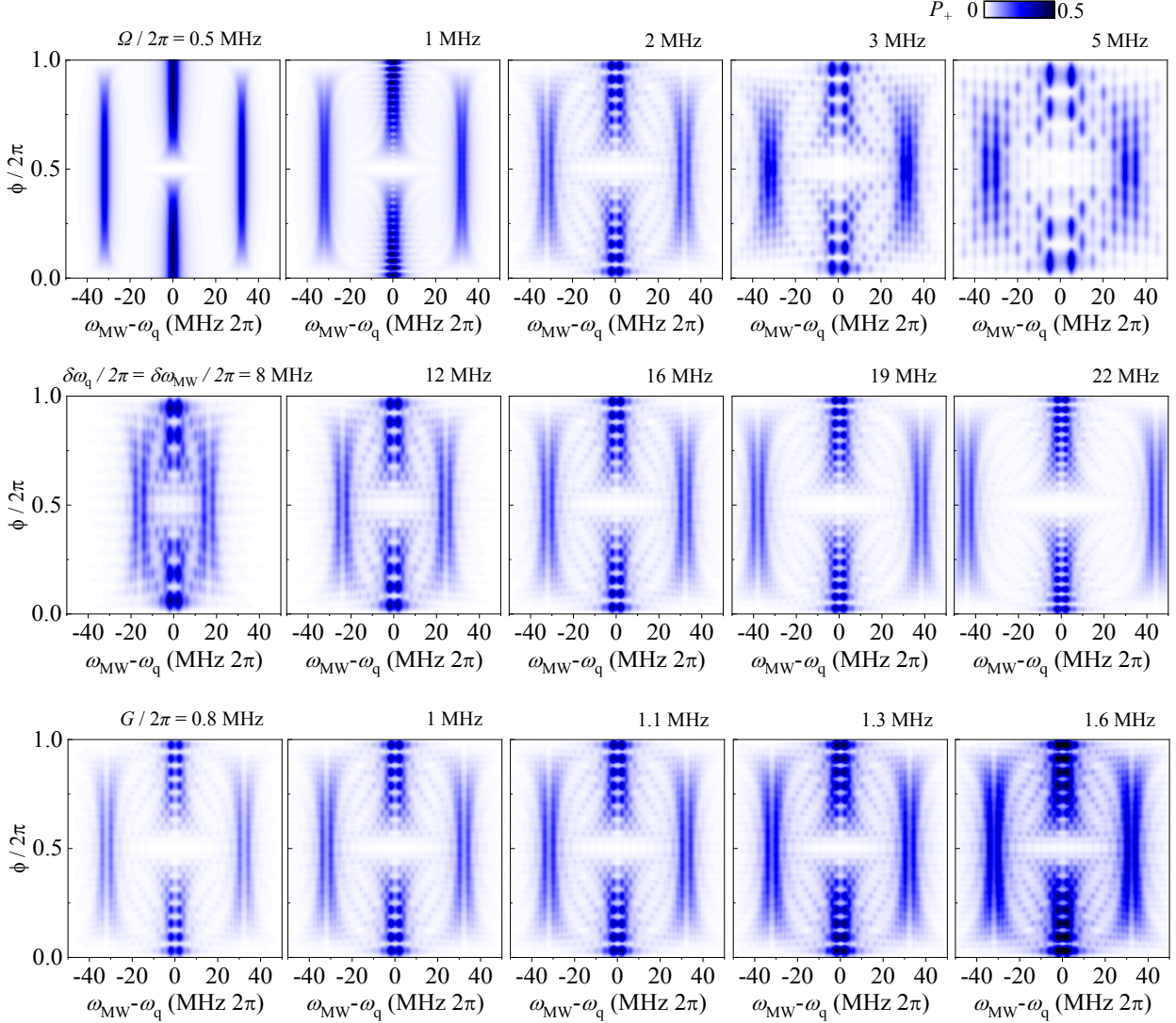


FIG. S7: Upper-level occupation probability P_+ as a function of the frequency detuning ($\omega_{MW} - \omega_q$) and the phase difference ϕ , for several values of the modulation frequency Ω (upper row), amplitude of energy-level modulation $\delta\omega_q$ (middle row), and driving amplitude G (lower row).

2. Coherent regime

To describe the coherent regime, with $\Omega \gtrsim 2T_2^{-1}$, as in Fig. S6, we again use Eqs. (S7) and (S9) to plot the upper-level occupation probability P_+ in the general case, for the respective parameters. Figure S7 presents the appearance of the interference fringes, where the upper-level occupation probability rapidly changes between 0 and 1/2. This figure correctly reproduces the experimental data in Fig. S6. Note that the upper panels of Fig. S6

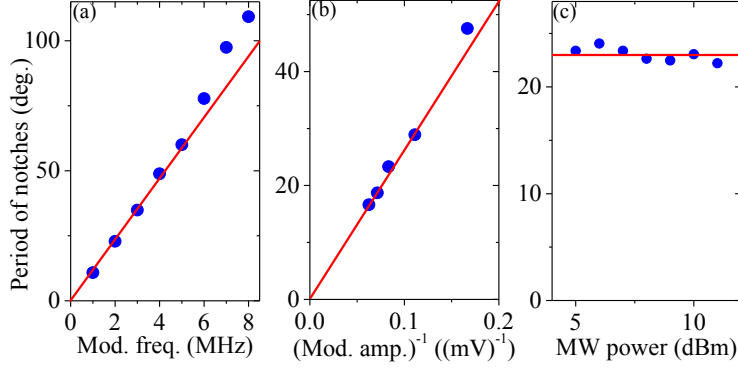


FIG. S8: Period of the notches (see Fig. 3 of the main text) as a function of the modulation frequency Ω , inverse modulation amplitude δV^{-1} , and the microwave power P_{MW} .

and Fig. S7 demonstrate how the interference fringes appear when increasing the modulation amplitude, starting from $\Omega = 0.5 \text{ MHz} \cdot 2\pi < 2T_2^{-1}$.

We call “notches” the suppression of the resonance lines down to $P_+ = 0$, see Fig. 3 of the main text. From Eq. (S9) it follows that the distance between the notches is defined by

$$\Delta\phi/2\pi = \Omega/\delta\omega_{\text{MW}} \propto \Omega \quad \text{and} \quad \Delta\phi/2\pi = \Omega/\delta\omega_{\text{q}} \propto \delta\omega_{\text{q}}^{-1}, \quad (\text{S16})$$

if changing Ω and $\delta\omega_{\text{q}}$, respectively. Importantly, the distance between the notches is proportional to the modulation frequency Ω , inversely proportional to the modulation amplitude $\delta\omega_{\text{q}}$, and is independent of the driving amplitude G , where the latter is defined by the MW power P_{MW} . These relations are demonstrated in Fig. S8(a, b, and c), respectively.

3. Dynamics

So far, we considered the stationary solution in order to describe the experimentally observed data. The obvious success in this allows us to claim that we have both the correct physical explanation of what happens and also the correct parameters. Then, with this, we can go further and solve numerically the Bloch equations to demonstrate the dynamics of the upper-level occupation probability.

The time evolution of the upper-level occupation probability $P_+(t)$ for the coherent case, with $\Omega/2\pi = 2 \text{ MHz}$, is shown in Fig. S10. For this we solved the time-dependent Bloch equations numerically, with different initial conditions. In a few cycles, the transient dynam-

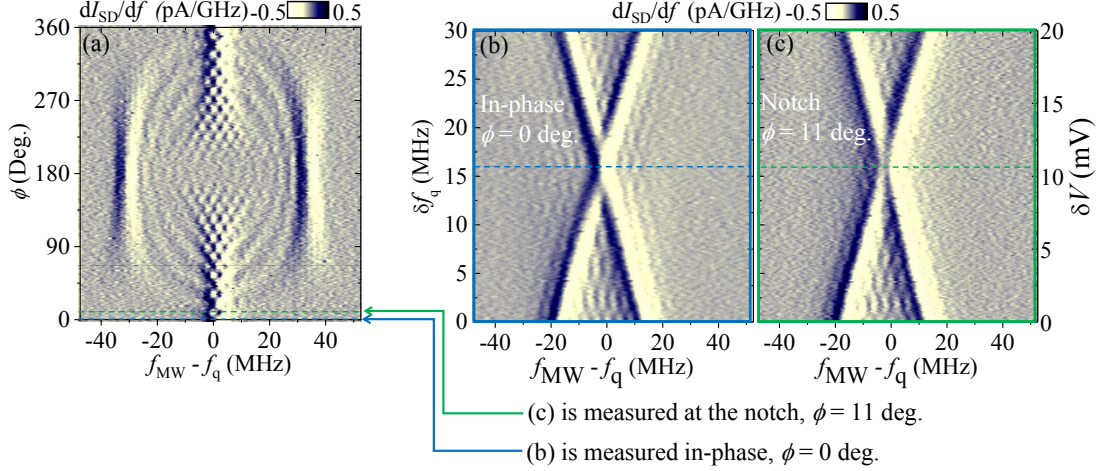


FIG. S9: Interference fringes in the dependence of the source-drain current I_{SD} for the X-shaped pattern. This is shown in (b) and (c) as a function of the frequency detuning ($f_{MW} - f_q$) and the amplitude δf_q of the energy-level modulation, for two values of the phase difference ϕ , which correspond to the lines shown in (a).

ics evolves into the stationary solution. Note that Fig. 3 of the main text and the graphs above show the time-averaged stationary solution, which corresponds to the upper-level occupation probability P_+ at times $t \gg T_{1,2}$. However, in principle, after preparing either the ground or excited state, we can start up our device following one of the trajectories in the main panel of Fig. S10 and quantify it by the extended efficiency e in the inset. The extended efficiency is introduced there so that $e = 1$ corresponds to a perfect engine, as in Fig. 1(a) of the main text, while $e = -1$ corresponds to a perfect refrigerator, as in Fig. 1(c). Coexistence and interference of these two cycles gives $e \in (-1, 1)$. A decoherence or complete mixing of these cycles leads to $e = 0$ and the system does not work as a heat engine anymore.

In order to see the dynamics in the experiment, after initializing the qubit, we would need a pulse-modulation of the drive frequency + qubit energy. The pulse length is expected to be about 0.1–1 μ s from the previous Rabi oscillation experiment (Ref. [28]). However, such experiments have not been possible because the current experimental setup does not have enough equipment to perform this pulsing. Thus, the experiments on the dynamics are outside of the scope of this paper. In the future, we would like to conduct the pulse experiments related to our calculated predictions, shown in Fig. S10.

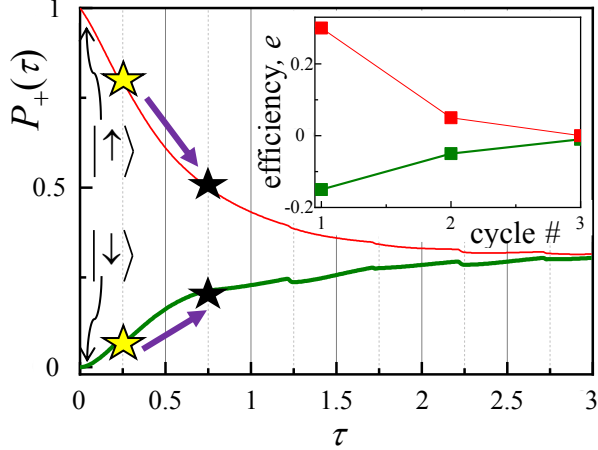


FIG. S10: Dynamics and the extended efficiency e . Evolution of the upper-level occupation probability P_+ , starting from the ground state (thick green curve) and the excited state (thin red curve). The inset shows the respective extended efficiency e , which is defined for each cycle as the difference of the probability at the beginning and the end of the small-energy-gap stage, shown by the yellow and black stars, respectively.

Results of calculations are further presented in Fig. S11 for (a) the incoherent ($\Omega < 2T_2^{-1}$) and (b) coherent ($\Omega \gtrsim 2T_2^{-1}$) cases. In Fig. S11(a) the red and green curves correspond to the resonant driving during either the high-energy stage or the low-energy stage, which describe the upper or lower panels in Fig. 1 of the main text, respectively. Thin dashed and dotted curves illustrate the situation of starting from a different initial condition, which is being in the excited state. *Note that during the excitation, the system is first resonantly excited and then relaxes to the stationary solution, which makes a kink at the beginning of the “ON” stage.* In Fig. S11(b), the numbers $n = 1, 2, 3$ denote the parameters, taken for the first three resonant points in Fig. 3(e) of the main text around $\delta\omega = 0$ and counted from the bottom. *At long times, $t \gg T_{1,2}$, after the transient dynamics finishes, the upper-level occupation probability tends to its stationary solution P_+ . This is defined by the competition of excitation and relaxation, and is given by Eq. (S7), which gives $P_+ \leq 1/2$.*

In Fig. S12 we present the calculated extended efficiency e , which is defined for each cycle as the difference of the probability at the beginning and the end of the small-energy-gap stage, see this in Fig. S11, shown by the arrows. Figure S12 is calculated for the incoherent regime, for the same parameters as Fig. S4. Note that for the stationary solution, the extended

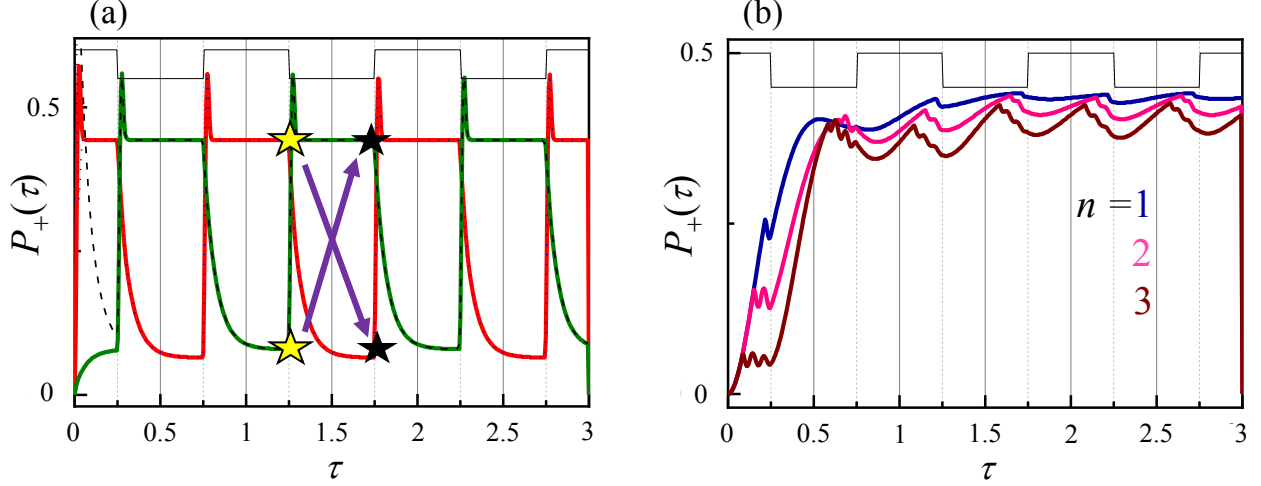


FIG. S11: Incoherent and coherent dynamics. The upper-level occupation probability P_+ is plotted as a function of the dimensionless time $\tau = \Omega t/2\pi$. Thin solid lines are given as a guide for the eye in order to mimic the large- and small-energy gap stages. The square modulation frequency $\Omega/2\pi$ is 0.2 MHz for (a) and 2 MHz for (b).

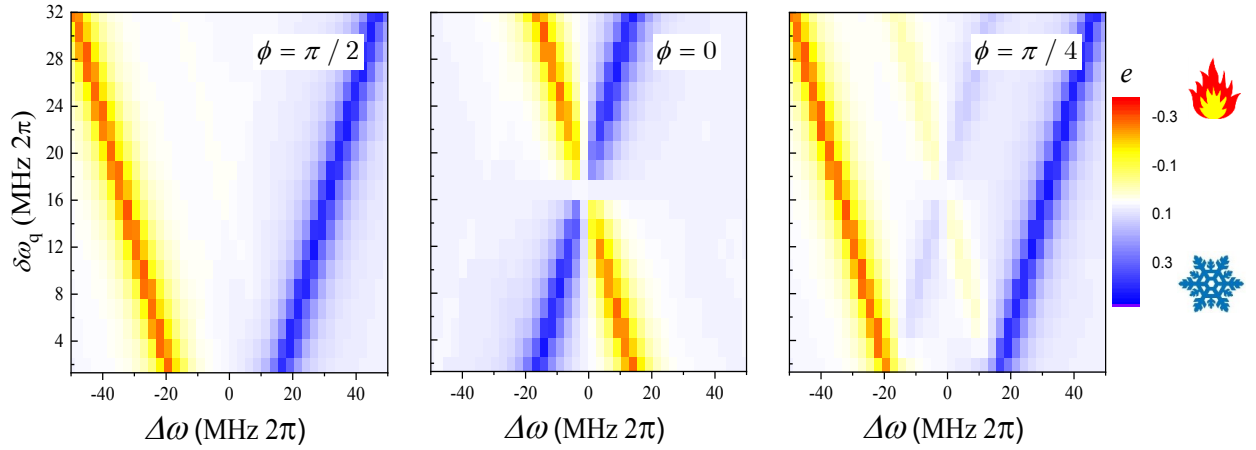


FIG. S12: Extended efficiency e in the incoherent regime. This is calculated for the same parameters as Fig. S4, as a function of the microwave frequency detuning $\Delta\omega = \omega_{\text{MW}} - \omega_q$ and the energy-level modulation amplitude $\delta\omega_q$.

efficiency e is close to 0 in the coherent regime (see Fig. 4 of the main text), while it displays both the heat-engine and refrigerator regimes in the incoherent regime, as shown in Fig. S12 by the red and blue colours, respectively.